

pubs.acs.org/IECR Article

Kinetic Origins of High Selectivity of Metal Phosphides for Ethane Dehydrogenation

Jeonghyun Ko, Hanyu Ma, and William F. Schneider*



Cite This: Ind. Eng. Chem. Res. 2022, 61, 12083-12091



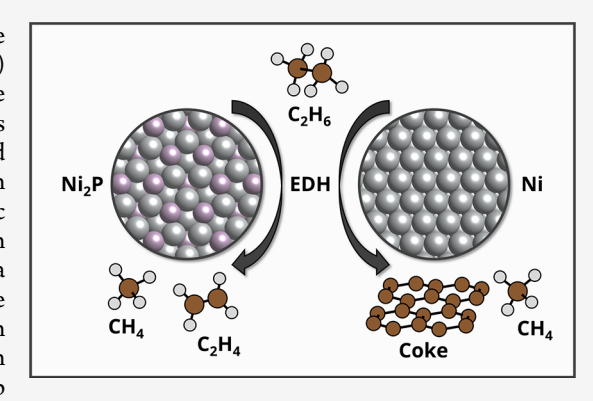
ACCESS

Metrics & More

Article Recommendations

Supporting Information

ABSTRACT: Supercell density functional theory (DFT) calculations are used to create and exercise complete ethane dehydrogenation (EDH) reaction networks over Ni(111) and Ni₂P(001). EDH intermediates are predicted to be more weakly bound to Ni₂P than to Ni, with the differences being the greatest for deeply dehydrogenated intermediates. Both C–H and C–C bond cleavage activation energies are generally greater on Ni₂P than Ni. The implications of these differences are explored through microkinetic models that incorporate a pathway for carbon growth. Ethylene formation rates and selectivities are predicted to be greater over Ni₂P than Ni across a wide range of temperatures. Ni is predicted to be more susceptible to coke generation. Ethane activation exerts the greatest degree of rate control on both materials; in contrast, the competition between ethylene desorption and dehydrogenation controls selectivity on Ni, while no single step



dominates selectivity on Ni₂P. Results are consistent with previously reported observations, highlight the distinct and active contributions of phosphorus to phosphide surface chemistry, and highlight the role of coking pathways on predicted kinetics.

1. INTRODUCTION

The abundance of shale resources in the United States has resulted in natural gas liquids (NGLs) production to exceed domestic consumption. ^{1–4} Ethane comprises the largest fraction by volume of NGLs, and dehydrogenation to ethylene could be the first step in transforming this NGL into a petrochemical feedstock. ³ Ethane steam crackers are energy- and capital-intensive ^{5,6} while oxidative dehydrogenation wastes potentially valuable hydrogen. Thus, alternative routes to direct ethane dehydrogenation are desirable.

Catalytic ethane dehydrogenation (EDH, $C_2H_6 \rightarrow C_2H_4 + H_2$) could provide an alternative to steam cracking that could be performed in smaller and local processing plants. However, because the reaction is highly endothermic, temperatures of >750 °C are required to reach \geq 50% conversion at atmospheric pressure. Catalyst selectivity and resistance to coke are both challenging under these harsh conditions, and thus EDH catalysis is not practiced commercially today.

Precious metals are active for EDH, and alloying with a second element has been shown to suppress catalyst deactivation. The isolation of active metal ensembles in these alloys is thought to be important in avoiding undesirable side reactions and catalyst coking. In particular, the alloying of Sn, In 2 Zn, In or In into Pt or Pd is observed to improve selectivity and catalyst stability. Density functional theory (DFT) models have been used to uncover the origins of these effects. In Hook et al. compared C-H and C-C bond cleavage pathways on Pt(111) and Pt_xSn(111) (x = 1, 3), thought to be important in determining selectivity toward ethylene versus coke. The alloys

are found to have higher barriers for both C-H and C-C bond cleavage and lower ethylene desorption energies, promoting the desired dehydrogenation over coke. C-C bond activation is also predicted to be more sensitive to Pt ensemble size than C-H activation, again providing protection against coke. A similar finding was recently reported by Hansen et al., ¹⁹ who developed microkinetic models for EDH on Pt and Pt₃Sn. Sn addition again is observed to suppress C-C bond cleavage, leading to coke resistance.

Metal phosphides—ordered, stoichiometric compounds of transition metals with phosphorus—in principle provide the same type of site isolation present in metal alloys. Many experimental studies suggest metal phosphides as potentially selective and robust EDH catalysts. $^{20-24}$ In particular, phosphorus incorporation into Ni^{25} and Co^{26} has been observed to lead to improved EDH selectivity and resistance to coke. DFT calculations on a $\mathrm{Ni}_2\mathrm{P}(001)$ model 25 indicate that surface P participates in adsorbate binding and C—H bond activation, and that deep dehydrogenation steps have higher activation energies than does ethylene desorption. In addition, P imparts coke resistance by reducing the binding energies of hydrocarbon

Special Issue: In Honor of Joan F. Brennecke

Received: June 9, 2022 Revised: July 28, 2022 Accepted: July 28, 2022 Published: August 2, 2022





fragments relative to the more active Ni catalyst. Thus, P incorporation has a direct influence on activity, selectivity, and coke resistance. Previous DFT calculations rationalized this influence based on comparisons to comparable reaction steps on Ni. Dehydrogenation does not need to follow similar pathways on metals and phosphides, and a full microkinetic analysis incorporating reaction conditions is necessary to reveal the kinetic and mechanistic origins of the performance of metal phosphides under EDH conditions.

Coke is believed to arise during catalytic dehydrogenation from unwanted deep dehydrogenation and C–C bond scission of surface reaction intermediates. Deep dehydrogenation can lead to on-surface or subsurface C atoms that aggregate into graphene islands^{27–29} and that ultimately physically cover catalytic surfaces. Coke formation can be observed in high-resolution transmission electron microscopy experiments,^{29–33} and on a Pt/MgO catalyst, for instance, is observed to appear over time periods of minutes under EDH conditions.²⁹ The incorporation of carbon growth pathways is an important element of EDH microkinetic models.

Here, we report DFT calculations of EDH reaction pathways and side-reaction on model Ni(111) and Ni₂P(001). Then, we develop microkinetic models that incorporate a simplified carbon growth model to predict EDH reaction rates and product selectivity over a wide range of conditions. We compare models that include and exclude carbon growth to highlight the differential impact on overall EDH performance. The results highlight the kinetic origins of the improved EDH performance on P-containing catalysts over Ni-only ones.

2. COMPUTATIONAL DETAILS

DFT calculations were performed with the Vienna Ab Initio Simulation Package (VASP) $^{34-36}$ Exchange-correlation energies were treated within the generalized gradient approximation (GGA), 37 using the Perdew–Burke–Ernzerhof (PBE) functional. Bulk lattice parameters were computed at a plane wave cutoff of 520 eV and slab calculations with a wave cutoff of 400 eV. Ni calculations were performed spin-polarized; in test calculations, we found Ni $_2$ P to have a negligible magnetic moment.

Bulk Ni is face-centered cubic, and the GGA-optimized lattice constant is close to the experimental value of a=3.52 Å. 38 Bulk Ni $_2$ P is hexagonal (space group $P\overline{6}2m$) and consists of alternating Ni $_3$ P $_2$ and Ni $_3$ P $_1$ planes stacked along the [001] direction. GGA-computed lattice parameters of a=b=5.88 Å and c=3.37 Å are close to the experimental values of a=b=5.86 Å and c=3.37 Å. 39 The Ni(111) and Ni $_2$ P(001) surfaces were modeled with five- and six-layer slabs, respectively, with a vacuum spacing of 15 Å. The bottom three layers were fixed at their bulk positions and the remaining layers and adsorbates fully relaxed. (3 \times 3) and (1 \times 1) surface unit cells were employed for Ni(111) and Ni $_2$ P(001), respectively, as shown in Figures 1a and 1b, respectively. Monkhorst—Pack grids 40 of 3 \times 3 \times 1 and 7 \times 7 \times 1 k-points were selected for Ni(111) and Ni $_2$ P(001) from k-point convergence test calculations.

Geometries were relaxed to minima using the conjugate gradient algorithm until forces on unconstrained atoms were <0.02 eV/Å. The climbing image-nudged elastic band (CI-NEB) method was employed to determine the minimum energy paths and calculate the activation energies for surface reactions.⁴¹ Vibrational spectra were obtained by calculating the Hessian matrix with finite differences of 0.015 Å. Each transition state was verified to have a single imaginary frequency

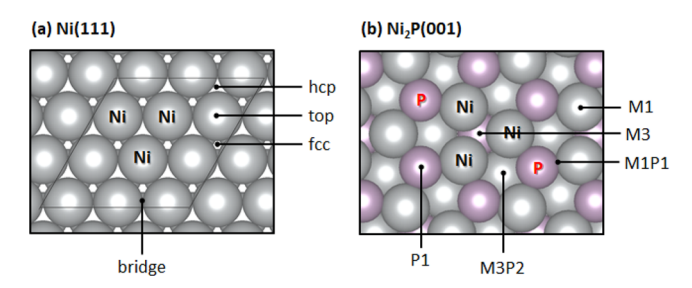


Figure 1. Top views of (a) the Ni(111) and (b) A-termination of Ni₂P(001). Computational supercells are indicated with light lines, Ni atoms shown in gray, P shown in lavender, and adsorption sites labeled on each surface. [Reprinted with permission from ref 25. American Chemical Society, Washington, DC.]

along the reaction coordinate (see Table S2 in the Supporting Information). Zero-point energies (ZPE) are included in all reported energy differences.

The enthalpies of adsorption are assumed to be the ZPE-corrected DFT energies. The entropies of gas molecules are from NIST-JANAF thermochemical tables, ⁴² and the entropies of adsorbates were estimated from the harmonic oscillator approximation. Vibrational modes with frequencies of <50 cm⁻¹ are often ignored or replaced with a cutoff frequency of 50 cm⁻¹ to avoid unphysical entropies from the harmonic oscillator approximation. All calculated frequencies are >50 cm⁻¹ here and thus all modes are treated harmonically.⁴³

Reactions rate constants (k) were computed using harmonic transition-state theory (TST):

$$k(T) = \frac{k_{\rm B}T}{h} \exp\left(\frac{\Delta S^{\circ}(T)}{k_{\rm B}}\right) \exp\left(-\frac{E_{\rm a}}{k_{\rm B}T}\right)$$
(1)

 $k_{\rm B}$ is the Boltzmann constant, h is the Planck constant, $\Delta S^{\circ}(T)$ is the entropy difference, and E_a is the zero-point-corrected energy difference between the transition state and reactants. In adsorption/desorption reactions, the entropies of transition states are assumed to be the same as the corresponding adsorbates. The assumptions on entropies of adsorption/ desorption transition states impact the absolute values of adsorption/desorption rates and the predicted overall rates. The relative rates among materials or at different temperatures, however, are not sensitive to these assumptions. 44 The steadystate coverages and rates at constant pressures were solved with a mean-field microkinetic model, as detailed in our previous works. 45,46 In brief, the pressures of gas phase species are fixed and the reactions are evaluated without the presence of products. The total coverage on the surface is conserved. The changes of surface coverages with time are described by ordinary differential equations (ODEs) parametrized with rate constants calculated from eq 1, which were first solved using numerical methods. The coverages solved from ODEs were further used as initial guesses to solve a system of algebraic equations to generate converged coverages and rates at steady state.

3. RESULTS AND DISCUSSION

3.1. Adsorption and Reactions on Ni(111) and Ni₂P-(001). Figure 2 summarizes the possible C_2 and C_1 species deriving from EDH on a catalytic surface and their associated interconnectivity by elementary reactions. We computed the relaxed structures of all species, considering the four adsorption sites on Ni(111) and five on Ni₂P(001)-A shown in Figure 1. DFT-computed adsorption structures are provided as CON-

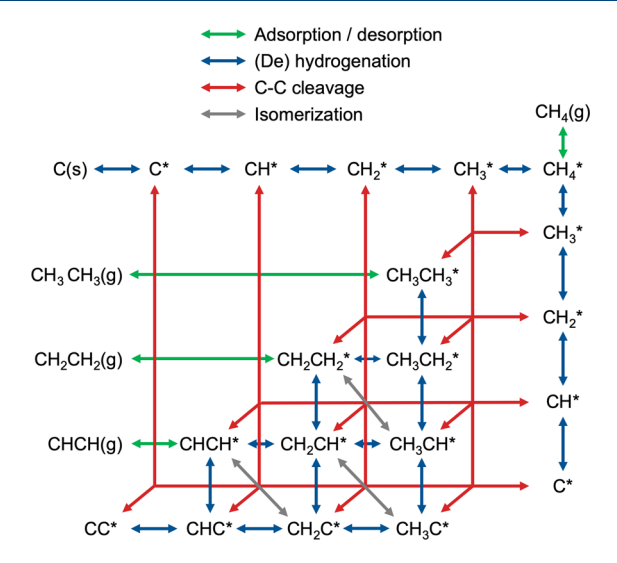


Figure 2. EDH reaction network. Adsorption and desorption are shown as green arrows. C—H and C—C bond cleavage steps are denoted by blue and red arrows, respectively. Isomerization steps are indicated with gray arrows.

TCAR files in an external repository.⁴⁷ Preferred (lowest energy) adsorption sites and corresponding adsorption energies, defined relative to gas-phase H₂ and CH₄, at those preferred binding sites are summarized in Table 1 and in Figures S1 and S2

Table 1. Adsorption Energies (E_{ads}) and Sites of Reaction Intermediates on Ni(111) and Ni₂P(001)

	Ni(111)		Ni ₂ P(001)	
adsorbate	sitea	$E_{\rm ads}^{b}$ (eV)	site ^a	$E_{\rm ads}^{b}$ (eV)
CH ₃ *	fcc	0.37	P1	0.47
CH ₂ *	fcc	0.77	M1P1	0.99
CH*	fcc	0.86	M3	1.31
C*	hcp	1.78	M3	2.53
H*	fcc	-0.52	M3	-0.56
CH ₃ CH ₂ *	fcc	1.23	P1	1.08
CH ₂ CH ₂ *	top-fcc	1.34	M1	1.44
CH ₃ CH*	fcc	1.33	M1P1	1.55
CH ₂ CH*	fcc-top	1.76	M3-M1	1.92
CH ₃ C*	fcc	1.15	M3	1.52
CHCH*	hcp-fcc	1.47	M2-M2	2.13
CH ₂ C*	fcc	1.85	M3-M1	2.09
CHC*	fcc-hcp	2.22	M3-M2	2.80
CC*	fcc-hcp	3.16	M3-M1P1	4.38

"Adsorption sites described in Figure 1 $^bE_{ads}$ s calculated relative to the gas-phase energies of H_2 , CH_4 , respectively. All values are zero-point-corrected.

in the Supporting Information. Binding energies on Ni₂P are reported as a parity plot against Ni binding energies in Figure 3a. Energies are generally shifted upward, to weaker binding, on Ni₂P(001) relative to Ni(111). This trend is particularly pronounced (up to 1.2 eV) for more deeply dehydrogenated species, including (CH₃C, CHCH, CHC, CC) or C1 (C, CH) species. These trends are consistent with those reported previously and traced to downshifts in the Ni *d*-band on the phosphide relative to Ni accompanying P incorporation. ²⁵ Also notable is the preference for sp³ species to bind to P over Ni sites on the phosphide. Phosphorus sites are not expected to be innocent to EDH surface chemistry, and thus binding energy

trends cannot be rationalized by a metal-centered d-band shift alone.

The differences in Figure 3a are manifested as shifts in reaction energies, as reported in Table S1 in the Supporting Information. Reaction energies are reported relative to surface species at infinite separation, and reactions 1–16, 17–26, 27–29, and 30 correspond to C–H bond cleavage, C–C bond cleavage, isomerization, and carbon growth steps, respectively. Consistent with Figure 3a, reactions leading to more deeply dehydrogenated products are less favorable on Ni₂P than on Ni.

We computed reaction pathways, transition states, and associated activation energies for all reported reaction steps. Several initial and final states, including the lowest and local minima positions, were used as starting points and end points to find transition states for each reaction step. We found multiple transition-state configurations, depending on initial and final states. Here, we report and use the lowest-energy transition-state configurations. Each transition state was confirmed to have a single imaginary frequency (see Table S2 in the Supporting Information). Computed reaction pathways including initial, transition, and final states are provided as CONTCAR files in an external repository.⁴⁷ Activation energies were calculated by subtracting the energy of a transition state from the energies of reactants at infinite separation. Computed activation energies are also summarized in Table S1.

C–H scission barriers on Ni₂P are plotted against those on Ni in Figure 3b and for C–C scission barriers in Figure 3c. C–H scission barriers are generally shifted upward on Ni₂P, relative to Ni, except for the activation of ethane $(C_2H_6(g)+^*\leftrightarrow C_2H_5^*+H^*)$ and of methane $(CH_4(g)+^*\leftrightarrow CH_3^*+H^*)$; both materials are thus expected to have similar intrinsic reactivity. Trends are similar but differences are even greater for C–C bond scission on Ni₂P relative to Ni, suggesting a greater resistance of Ni₂P for generation of methane or of coke precursors. Isomerization barriers (reactions 27–29 in Table S1) are similar and largely independent of material.

3.2. Microkinetic Analysis. We built mean-field microkinetic model including full EDH pathways on Ni(111) and Ni₂P(001). Elementary steps are summarized in Figure 2 and Table S1. We assumed that adsorbate diffusion is much more rapid than surface reaction⁴⁸ and surface species have the same entropy. The surface coverages at steady state are calculated with a mean-field microkinetic model⁴⁹ by solving ODEs. Reaction rates are calculated through obtained surface coverages.

We incorporated a simplified carbon growth model illustrated in Figure 4, in which adsorbed carbon can react to form graphite and liberate a surface site:

$$C^* + nC_{\text{graphite}} \leftrightarrow (n+1)C_{\text{graphite}} + *$$
 (2)

This model allows us to incorporate a carbon growth channel that does not chemically poison the surface, consistent with the ability of Ni to catalyze carbon growth. It does not incorporate physical site blockings that can accompany coke formation on supported catalysts. We decomposed the energy of rxn 2 into the DFT-computed energy of $C^*+2H_2\to CH_4+^*$ and the JANAF-NIST-tabulated energy of carbon growth from methane, $CH_4\to C_{graphite}+2H_2.^{42}$ We assumed the forward activation energy of rxn 2 to be that computed for C–C bond formation, $2C^*\to C_2^*+^*$, and enforced thermodynamic consistency to determine the reverse activation energy. The resultant activation energy on Ni (1.0 eV) is somewhat less than that determined from more-detailed models of multiple pathways and Ni surface

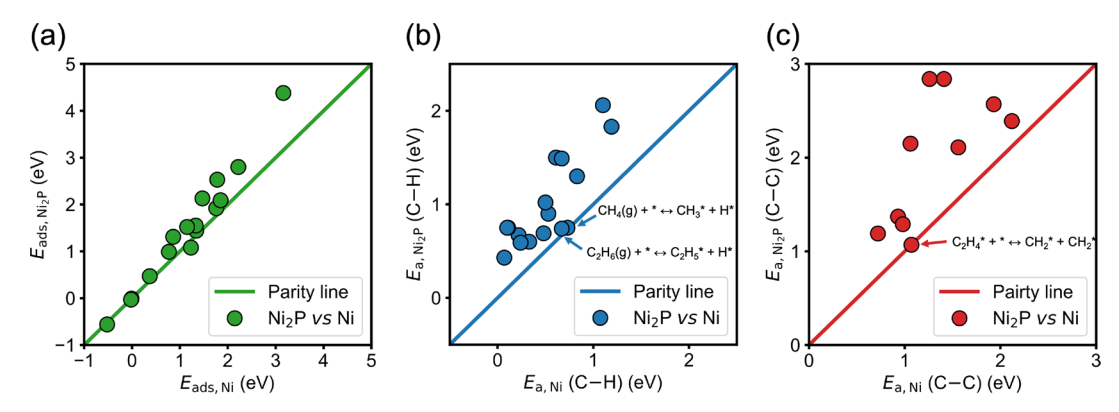


Figure 3. Parity plots of (a) adsorption energy (E_{ads}), (b) C–H and (c) C–C bond cleavage on Ni(111) and Ni₂P(001). Adsorption energies (E_{ads}) of H, and the C1 and C2 species, are calculated relative to the gas-phase energies of H₂ and CH₄, respectively.

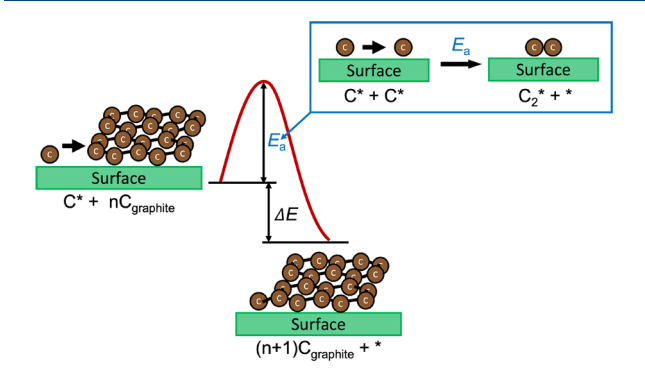


Figure 4. Schematic of kinetic model for addition of adsorbed carbon to a growing graphene sheet.

morphologies (1.5 eV). 50,51 While absolute activation energies are sensitive to these details, we expect the difference between Ni and Ni₂P to be preserved and the model to thus capture the difference between these two materials.

We solved the full reaction network including the simplified carbon growth model on Ni(111) and Ni₂P(001) for production rate and selectivity over a wide range of temperatures (750–1000 K) and $P_{\text{C}_2\text{H}_6} = P_{\text{H}_2} = 0.5$ bar, typical of EDH. Figure 5a reports the ethylene production rate versus temperature as an Arrhenius plot. The steady-state coverages over Ni(111) and Ni₂P(001) are shown in Figure S3 in Supporting Information. Rates are almost linear on the Arrhenius plot, corresponding to apparent activation energies of ~130 kJ/mol on both materials.

Furthermore, rates on $Ni_2P(001)$ are ~ 1 order of magnitude greater than on Ni(111) over the entire temperature range. As the initial $H-C_2H_H$ activation step is computed to have a higher intrinsic rate on Ni(111) than on Ni_2P , this higher activity reflects kinetic steps beyond that initial activation.

Figures 5b and 5c report product selectivities at zero conversion on Ni(111) and Ni₂P(111), respectively, versus temperature. We define selectivity as the ratio of the rate of a product i over the sum of the rates of C_2H_4 , C_2H_2 , CH_4 , and C(graphite):

selectivity (i) =
$$\frac{\nu_{i}r_{i}}{2r_{C_{2}H_{4}} + 2r_{C_{2}H_{2}} + r_{CH_{4}} + r_{C(graphite)}}$$
 (3)

where r_i is the formation rate of species i, $\nu_i = 1$ for CH₄ and C_{graphite} and $\nu_i = 2$ for C₂H₄ and C₂H₂. Selectivity on Ni is almost entirely relative to carbon across the entire temperature range, with small amounts of CH₄ at the lowest temperature and ethylene at somewhat higher temperature. In contrast, essentially no coke is predicted to form on Ni₂P; rather, selectivity is almost entirely relative to ethane at the lower temperatures, transitioning to CH₄ as temperature increases. The results compare favorably with experimentally reported 0% and 80% ethylene selectivities at 3% conversion on Ni/SBA-15 and Ni₂P/SBA-15, respectively, at the same partial pressures at 873 K.²⁵

To understand the origins of these differences, we performed reaction flux analyses at 873 K on the two reaction networks. Figure 6a reports the direction and net flux of every reaction step that has a normalized rate of \geq 0.01 for the rate of ethane

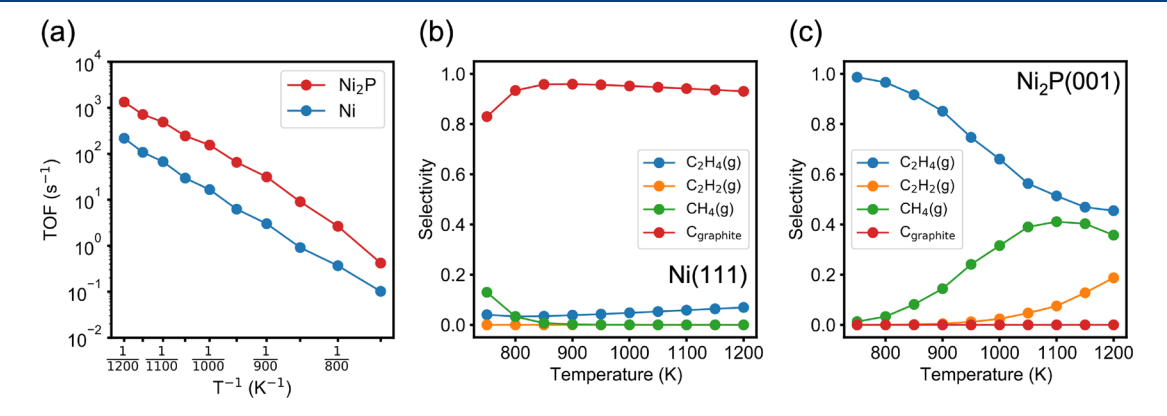


Figure 5. (a) Reaction rate against reciprocal temperature on Ni(111) and Ni₂P(001) at 0.5 bar C_2H_6 and H_2 for a microkinetic model including carbon growth. Selectivities on (b) Ni(111) and (c) Ni₂P(001) versus temperature at 0.5 bar C_2H_6 and H_2 .

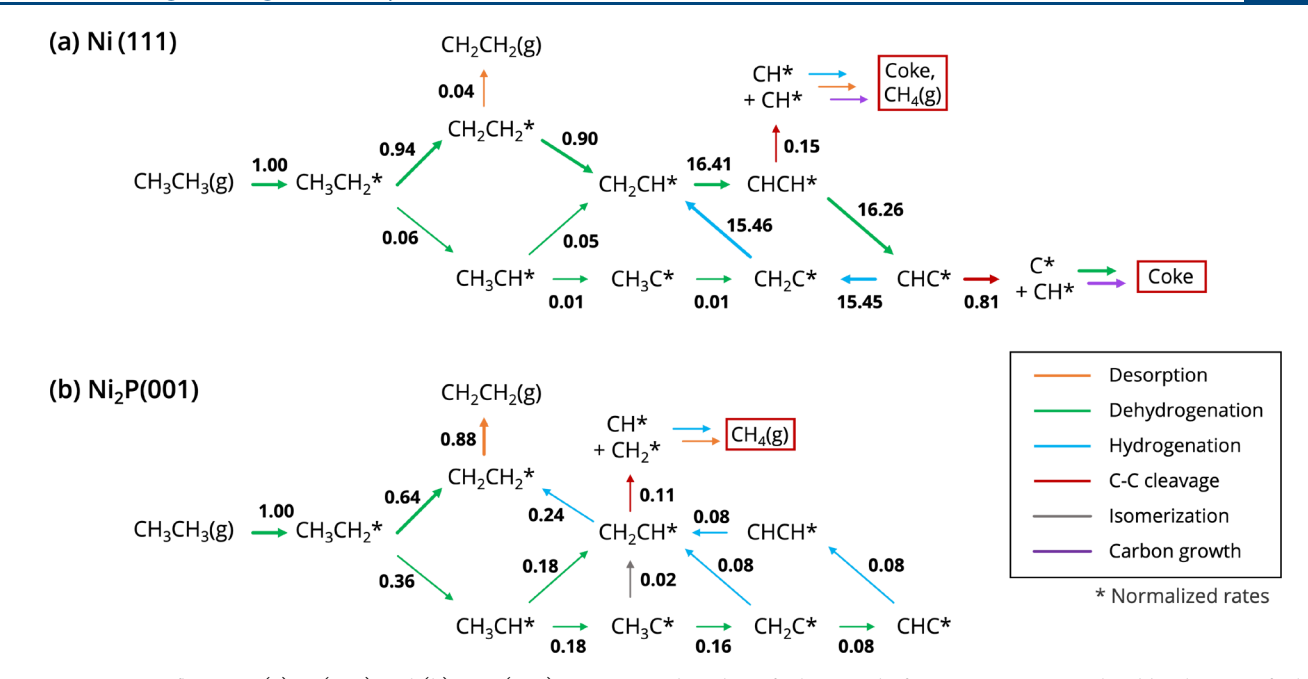


Figure 6. Reaction fluxes on (a) Ni(111) and (b) Ni₂P(001) at 873 K and 0.5 bar of ethane and of H_2 . Rates are normalized by the rate of ethane consumption. Arrows indicate the directions of net rates of each elementary step. Reaction fluxes with net rates <0.01 are not shown. Colors represent different types of reactions.

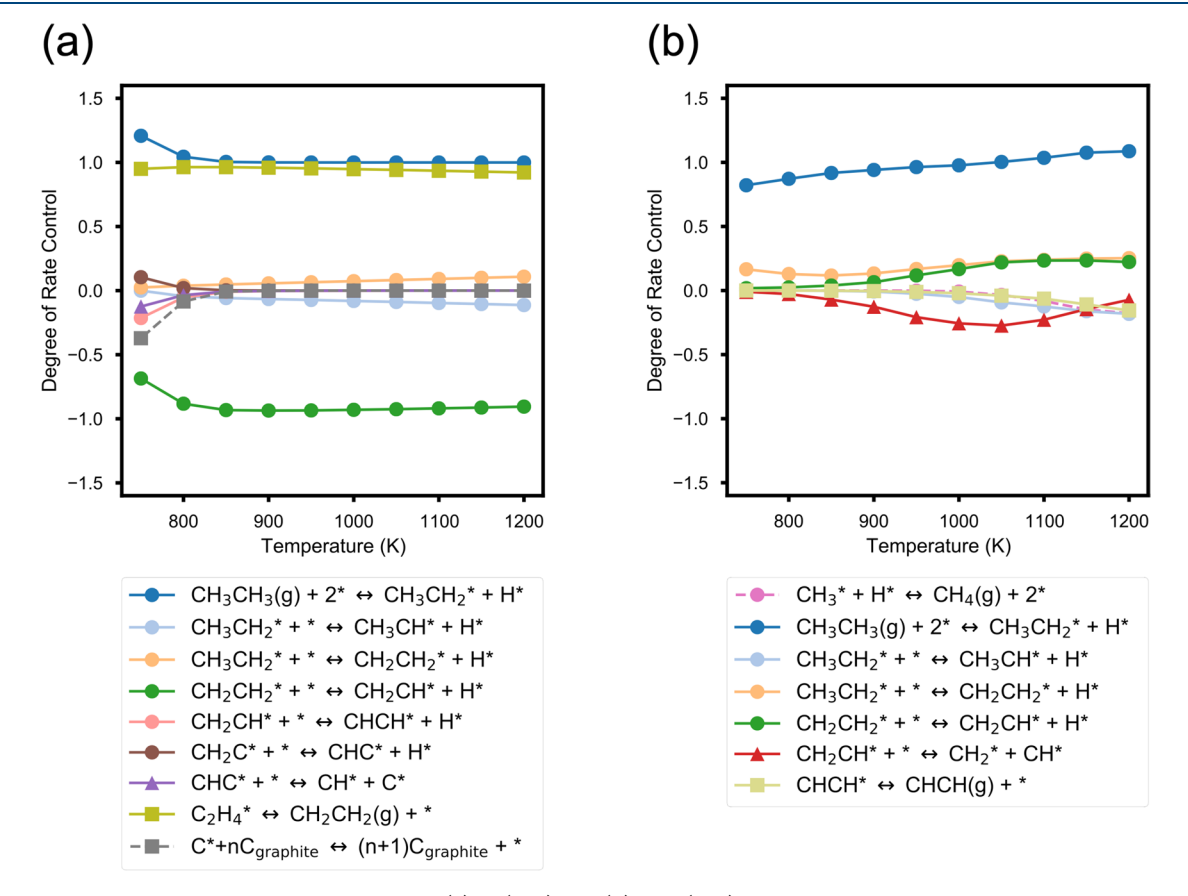


Figure 7. Degree of ethylene generation rate control on (a) Ni(111) and (b) Ni₂P(001) at 0.5 and 0.5 bar of C₂H₆ and H₂, respectively.

consumption, color-coded by the nature of the step, on Ni(111). Ethane activation forms surface ethyl which is then dehydrogenated to ethylene. The primary branch point, then, is between ethylene desorption and further dehydrogenation steps, all of which ultimately lead to coke. On Ni₂P (Figure 6b), in contrast,

surface ethyl is predicted to dehydrogenate to adsorbed ethylene or ethylidene (CH_3CH^*). While the former leads directly to ethylene product, the latter is predicted to undergo a one-step C-H activation or a C-H rearrangement loop to dehydrogenated CH_2CH^* . C-C cleavage and hydrogenation then

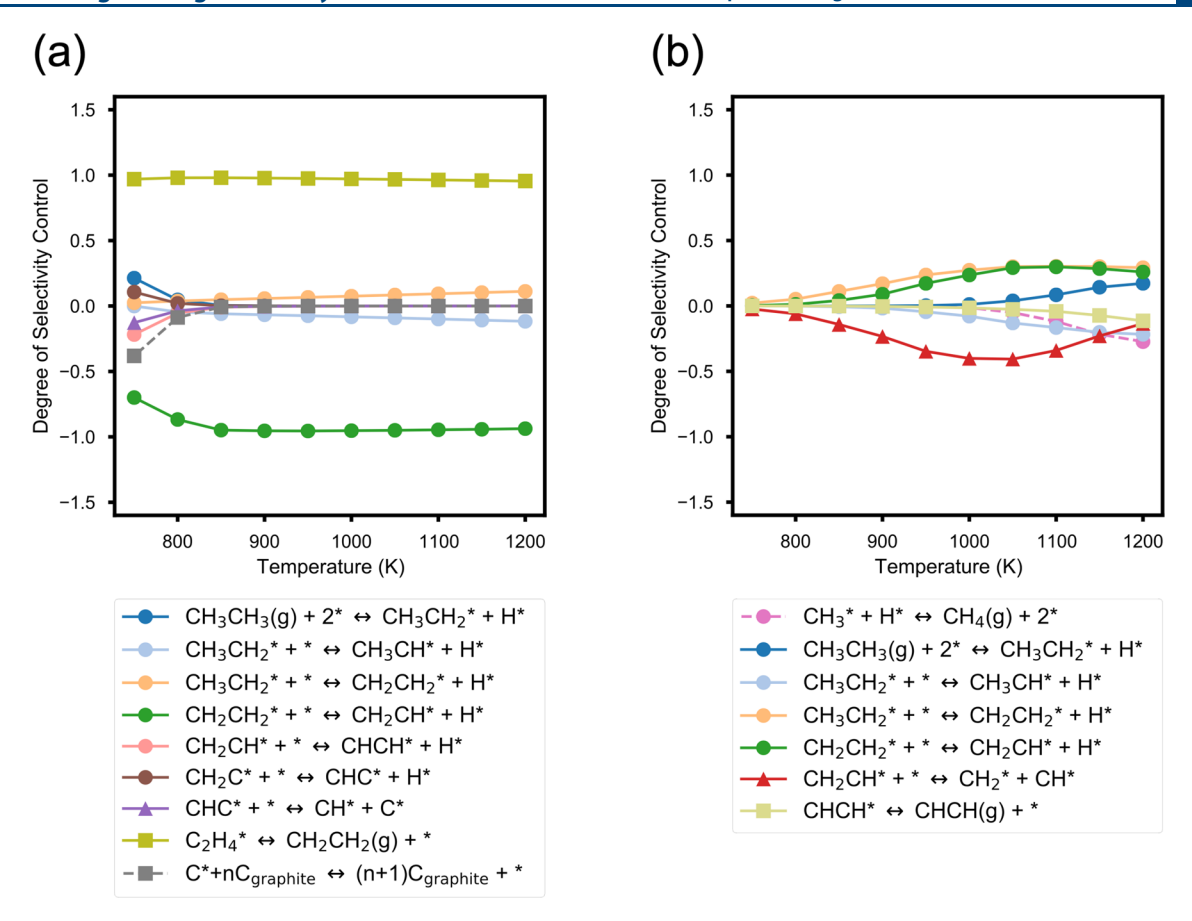


Figure 8. Degree of ethylene selectivity control on (a) Ni(111) and (b) Ni₂P(001) at 0.5 and 0.5 bar of C₂H₆ and H₂, respectively.

compete to produce either methane or adsorbed ethylene. This more-complex chemistry reflects the predicted activity of Ni_2P for catalyzing C–H rearrangements and the much weaker binding of C* to Ni_2P than to Ni, allowing C* hydrogenation to ethylene and methane to outcompete coke generation.

A degree of rate control (DRC) analysis provides insight into the factors controlling ethylene production rates. We defined the rate control sensitivity X_{RC} to an elementary step i, according to

$$X_{\text{RC},i} = \frac{k_{\pm i}}{r} \left(\frac{\partial r}{\partial k_{\pm i}} \right) \tag{4}$$

 $X_{RC.i}$ is calculated by finite difference, changing the forward (k_{+i}) and reverse (k_{-i}) rate constants of step *i* simultaneously by 1% and monitoring the fractional change of the ethylene production rate (r), relative to the reference rate, r_0 . DRC results using a 10% change in rate constant differ by <10% (see Figure S7 in the Supporting Information). Results for the two catalysts, as a function of temperature, are illustrated in Figures 7a and 7b. The sum of all DRC values is always unity. On Ni(111) (Figure 7a), the rate of ethylene production is controlled primarily by ethane activation $(C_2H_6(g) + 2^* \rightleftharpoons C_2H_5^* + H^*)$ and ethylene desorption $(C_2H_4^* \rightleftharpoons C_2H_4(g) + *)$, both of which have DRC values close to one at all temperatures. Coke formation has a negative effect on ethylene production at the lowest temperature, but across most of the temperature range, ethylene dehydrogenation $(C_2H_4^* + * \rightleftharpoons CH_2CH^* + H^*)$, which is the entrance into coke production, has the largest adverse effect on ethylene rates, with a DRC of \sim 1. On Ni₂P, in contrast, ethylene rates are almost entirely controlled by ethane activation across the entire temperature range, with a small positive and negative

contributions from various hydrogenation/dehydrogenation steps. C-C cleavage of vinylidene (CH_2CH^*), which leads to methane, has the most pronounced negative impact on ethylene production.

As shown in Figures 5b and 5c, selectivity toward ethylene is expected to be very different on Ni and Ni₂P. A DSC analysis highlights the origins of these differences. We define the DSC as the sensitivity of ethylene selectivity $X_{\rm SC}$, defined in eq 3, to variations in k_{+i} :

$$X_{\text{SC},i} = \frac{k_{\pm i}}{s} \left(\frac{\partial s}{\partial k_{\pm i}} \right) \tag{5}$$

Results as a function of temperature at 0.5 bar C_2H_6 and H_2 are shown in Figure 8. The sum of all DSC values is always zero. On Ni(111), ethylene desorption has the most positive impact on $X_{\rm SC}$ and ethylene dehydrogenation has the most negative impact at all but the lowest temperatures, consistent with the central role of adsorbed ethylene in the reaction flux analysis in Figure 6a. The DSC on Ni₂P tells a less straightforward story. At temperatures of <800 K, where selectivity to ethylene is ~100%, no single elementary step has a significant selectivity control impact. At higher temperatures, various dehydrogenations have small positive and negative impacts on selectivity, while vinylidene C–C cleavage, which leads to methane, has the most pronounced negative impact.

The role of coke in the relative predicted performance of the two materials is illustrated more clearly by comparing kinetics without inclusion of a carbon growth pathway. We used the same kinetic parameters but excluded the C* + nC_{graphite} \rightleftharpoons (n + 1)C_{graphite} + * step, so that C* has no direct exit channel from a

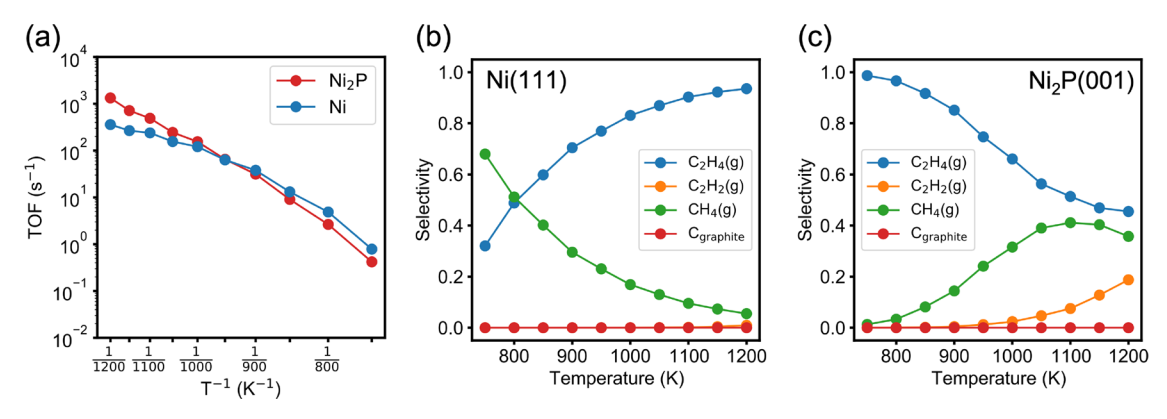


Figure 9. (a) Reaction rate against reciprocal temperature on Ni(111) and Ni₂P(001) at 0.5 bar C_2H_6 and H_2 for a microkinetic model excluding carbon growth. Selectivities on (b) Ni(111) and (c) Ni₂P(001) versus temperature at 0.5 bar C_2H_6 and H_2 .

surface site. Figure 9 shows the predicted ethylene generation rate and selectivity. The steady-state coverages are reported in Figure S4 in the Supporting Information. Results on $\mathrm{Ni_2P}$ are unchanged from that of the coke growth model. In contrast, results on Ni are quite different. The ethylene production rate increases to match that of $\mathrm{Ni_2P}$ across all but the highest of the temperature ranges. With coke excluded as a product, selectivity shifts from $\mathrm{CH_4}$ -dominated at lower temperature to ethylene-dominated at higher temperature. Carbon growth-excluded DRC for ethylene generation rate (Figure S5a in Supporting Information) and DSC for ethylene selectivity (Figure S6a in Supporting Information) rationalize this observation. At lower temperature $\mathrm{CH_4}$ formation significantly inhibits ethylene formation and selectivity but its contribution rapidly diminishes with increasing temperature.

These model results can be compared with EDH experiments over SBA-supported Ni and Ni₂P at 873 K and 3% conversion.² Ethylene production rates are reported to be an order of magnitude less on the Ni catalyst than the Ni₂P, consistent with results in Figure 5a. The simple slab representations of the two catalysts thus appears to capture relative rates, despite the approximate nature of the representation of the supported catalysts. Ethylene selectivity is reported to be >80% over Ni₂P/ SBA-15 and methane is reported to be the main secondary product, consistent with results in Figure 5c. In contrast, over the Ni/SBA-15 catalyst methane is the primary product. The carbon growth model appears to capture coke productivity but underestimate methane productivity, relative to observation. This difference suggests that the model overestimates the rate of carbon growth relative to the rate of carbon hydrogenation to methane, likely reflecting the underestimation of carbon growth activation energies and the inability of the Ni(111) model to capture the kinetics of methane generation on real Ni material. Nonetheless, the Ni(111) slab models combined with carbon growth do capture the key differences between the two catalyst classes.

4. CONCLUSIONS

We report a combination of DFT calculations and microkinetics models to illuminate the expected differences in ethane dehydrogenation performance of a Ni₂P catalyst, relative to Ni. The incorporation of phosphorus into a Ni catalyst generally decreases the binding energies of intermediates and increases the activation energies for their transformations, with effects most pronounced for species that are more deeply dehydrogenated. Microkinetic models show that these differences are

manifested in qualitative differences in dominant reaction pathways and features that control rates and selectivities. The ability of Ni to catalyze EDH is sensitive to the rate of $H-C_2H_H$ bond activation and to the selectivity between C2H4 desorption and C₂H₄ dehydrogenation, the latter of which is an irreversible step toward methane or coke. These observations are consistent with commonly used descriptors of dehydrogenation effectiveness. In contrast, model results suggest that C₂H₄ desorption has little effect on EDH rates or selectives on Ni₂P. Rather, because Ni₂P is effective at catalyzing hydrogenations and dehydrogenations, selectivity is primarily controlled by a competition between C-C bond cleavage and hydrogenation of vinylidene (C₂H₃*). The results indicate both the distinct catalytic chemistry of the phosphides and the need to define new descriptors for selecting optimal phosphides for EDH or other catalytic reactions.

ASSOCIATED CONTENT

Supporting Information

The Supporting Information is available free of charge at https://pubs.acs.org/doi/10.1021/acs.iecr.2c02044.

Summary of DFT-computed adsorption geometries of C1 and C2 species on Ni(111) and Ni₂P(001)-A; imaginary vibrational frequencies of transition states for elementary steps on Ni(111) and Ni₂P(001)-A (PDF)

AUTHOR INFORMATION

Corresponding Author

William F. Schneider — Department of Chemical and Biomolecular Engineering, University of Notre Dame, Notre Dame, Indiana 46556, United States; Department of Chemistry and Biochemistry, University of Notre Dame, Notre Dame, Indiana 46556, United States; orcid.org/0000-0003-0664-2138; Email: wschneider@nd.edu

Authors

Jeonghyun Ko — Department of Chemical and Biomolecular Engineering, University of Notre Dame, Notre Dame, Indiana 46556, United States

Hanyu Ma – Department of Chemical and Biomolecular Engineering, University of Notre Dame, Notre Dame, Indiana 46556, United States; oorcid.org/0000-0002-2193-6858

Complete contact information is available at: https://pubs.acs.org/10.1021/acs.iecr.2c02044

Author Contributions

These authors contributed equally to this work.

Notes

The authors declare no competing financial interest.

A Zenodo repository available at 10.5281/zenodo.6609601 contains the full set of INCARs for all calculations, CONTCARs for all the structures discussed in the manuscript, as well as Python code of microkinetic models and for figure plotting.

ACKNOWLEDGMENTS

This work was supported by the Engineering Research Centers Program of the National Science Foundation, under NSF Cooperative Agreement No. EEC-1647722. The computing resources and technical support for this work were provided by the Notre Dame Center for Research Computing.

REFERENCES

- (1) Bruijnincx, P. C. A.; Weckhuysen, B. M. Shale Gas Revolution: An Opportunity for the Production of Biobased Chemicals? *Angew. Chem., Int. Ed.* **2013**, *52*, 11980–11987.
- (2) Stangland, E. E. Shale Gas Implications for C2–C3 Olefin Production: Incumbent and Future Technology. *Annu. Rev. Chem. Biomol. Eng.* **2018**, *9*, 341–364.
- (3) Sattler, J. J. H. B.; Ruiz-Martinez, J.; Santillan-Jimenez, E.; Weckhuysen, B. M. Catalytic Dehydrogenation of Light Alkanes on Metals and Metal Oxides. *Chem. Rev.* **2014**, *114*, 10613–10653.
- (4) National Academies of Sciences, E.; Studies, D.; Technology, B.; Alper, J. The Changing Landscape of Hydrocarbon Feedstocks for Chemical Production: Implications for Catalysis: Proceedings of a Workshop; National Academies Press, 2016.
- (5) Wilczewski, W. U.S. Energy Information Administration EIA Independent Statistics and Analysis, 2015. Available via the Internet at: https://www.eia.gov/todayinenergy/detail.php?id/19771, accessed on July 26, 2022.
- (6) Ridha, T.; Li, Y.; Gençer, E.; Siirola, J.; Miller, J.; Ribeiro, F.; Agrawal, R. Valorization of Shale Gas Condensate to Liquid Hydrocarbons through Catalytic Dehydrogenation and Oligomerization. *Processes* **2018**, *6*, 139.
- (7) Cai, W.; Mu, R.; Zha, S.; Sun, G.; Chen, S.; Zhao, Z.-J.; Li, H.; Tian, H.; Tang, Y.; Tao, F. F.; Zeng, L.; Gong, J. Subsurface catalysis-mediated selectivity of dehydrogenation reaction. *Sci. Adv.* **2018**, *4*, DOI: 10.1126/sciadv.aar5418.
- (8) Nykänen, L.; Honkala, K. Density Functional Theory Study on Propane and Propene Adsorption on Pt(111) and PtSn Alloy Surfaces. *J. Phys. Chem. C* **2011**, *115*, 9578–9586.
- (9) Zellner, M.; Goda, A.; Skoplyak, O.; Barteau, M.; Chen, J. Trends in the adsorption and decomposition of hydrogen and ethylene on monolayer metal films: A combined DFT and experimental study. *Surf. Sci.* **2005**, *583*, 281–296.
- (10) Sheth, P. A.; Neurock, M.; Smith, C. M. First-Principles Analysis of the Effects of Alloying Pd with Ag for the Catalytic Hydrogenation of Acetylene-Ethylene Mixtures. *J. Phys. Chem. B* **2005**, *109*, 12449—12466.
- (11) Hook, A.; Massa, J. D.; Celik, F. E. Effect of Tin Coverage on Selectivity for Ethane Dehydrogenation over Platinum—Tin Alloys. *J. Phys. Chem. C* **2016**, 120, 27307—27318.
- (12) Galvita, V.; Siddiqi, G.; Sun, P.; Bell, A. T. Ethane dehydrogenation on Pt/Mg(Al)O and PtSn/Mg(Al)O catalysts. *J. Catal.* **2010**, 271, 209–219.
- (13) Wu, J.; Peng, Z.; Bell, A. T. Effects of composition and metal particle size on ethane dehydrogenation over $Pt_xSn_{100-x}/Mg(Al)O$ (70 $\leq x \leq 100$. *J. Catal.* **2014**, *311*, 161–168.
- (14) Cybulskis, V. J.; Bukowski, B. C.; Tseng, H.-T.; Gallagher, J. R.; Wu, Z.; Wegener, E.; Kropf, A. J.; Ravel, B.; Ribeiro, F. H.; Greeley, J.; Miller, J. T. Zinc Promotion of Platinum for Catalytic Light Alkane Dehydrogenation: Insights into Geometric and Electronic Effects. *ACS Catal.* **2017**, *7*, 4173–4181.

- (15) Wegener, E. C.; Wu, Z.; Tseng, H.-T.; Gallagher, J. R.; Ren, Y.; Diaz, R. E.; Ribeiro, F. H.; Miller, J. T. Structure and reactivity of Pt–In intermetallic alloy nanoparticles: Highly selective catalysts for ethane dehydrogenation. *Catal. Today* **2018**, *299*, 146–153.
- (16) Yang, M.-L.; Zhu, Y.-A.; Zhou, X.-G.; Sui, Z.-J.; Chen, D. First-Principles Calculations of Propane Dehydrogenation over PtSn Catalysts. *ACS Catal.* **2012**, *2*, 1247–1258.
- (17) Sun, G.; Zhao, Z.-J.; Mu, R.; Zha, S.; Li, L.; Chen, S.; Zang, K.; Luo, J.; Li, Z.; Purdy, S. C.; Kropf, A. J.; Miller, J. T.; Zeng, L.; Gong, J. Breaking the scaling relationship via thermally stable Pt/Cu single atom alloys for catalytic dehydrogenation. *Nat. Commun.* **2018**, *9*, DOI: 10.1038/s41467-018-06967-8.
- (18) Peng, G.; Gerceker, D.; Kumbhalkar, M.; Dumesic, J. A.; Mavrikakis, M. Ethane dehydrogenation on pristine and AlO_x decorated Pt stepped surfaces. *Catal. Sci. Technol.* **2018**, *8*, 2159–2174.
- (19) Hansen, M. H.; Nørskov, J. K.; Bligaard, T. First principles microkinetic model of catalytic non-oxidative dehydrogenation of ethane over close-packed metallic facets. *J. Catal.* **2019**, 374, 161–170.
- (20) Bonita, Y.; O'Connell, T. P.; Miller, H. E.; Hicks, J. C. Revealing the Hydrogenation Performance of RuMo Phosphide for Chemoselective Reduction of Functionalized Aromatic Hydrocarbons. *Ind. Eng. Chem. Res.* **2019**, *58*, 3650–3658.
- (21) Pei, Y.; Cheng, Y.; Chen, J.; Smith, W.; Dong, P.; Ajayan, P. M.; Ye, M.; Shen, J. Recent developments of transition metal phosphides as catalysts in the energy conversion field. *J. Materi. Chem. A* **2018**, *6*, 23220–23243.
- (22) Rensel, D. J.; Rouvimov, S.; Gin, M. E.; Hicks, J. C. Highly selective bimetallic FeMoP catalyst for C–O bond cleavage of aryl ethers. *J. Catal.* **2013**, 305, 256–263.
- (23) Rensel, D. J.; Kim, J.; Jain, V.; Bonita, Y.; Rai, N.; Hicks, J. C. Composition-directed FeXMo2-XP bimetallic catalysts for hydrodeoxygenation reactions. *Catal. Sci. Technol.* **2017**, *7*, 1857–1867.
- (24) Cho, A.; Shin, J.; Takagaki, A.; Kikuchi, R.; Oyama, S. T. Ligand and Ensemble Effects in Bimetallic NiFe Phosphide Catalysts for the Hydrodeoxygenation of 2-Methyltetrahydrofuran. *Top. Catal.* **2012**, *55*, 969–980.
- (25) Ko, J.; Muhlenkamp, J. A.; Bonita, Y.; LiBretto, N. J.; Miller, J. T.; Hicks, J. C.; Schneider, W. F. Experimental and Computational Investigation of the Role of P in Moderating Ethane Dehydrogenation Performance over Ni-Based Catalysts. *Ind. Eng. Chem. Res.* **2020**, *59*, 12666–12676.
- (26) Muhlenkamp, J. A.; LiBretto, N. J.; Miller, J. T.; Hicks, J. C. Ethane dehydrogenation performance and high temperature stability of silica supported cobalt phosphide nanoparticles. *Catal. Sci. Technol.* **2022**, *12*, 976–985.
- (27) Zhao, Z.-J.; Chiu, C.-c.; Gong, J. Molecular understandings on the activation of light hydrocarbons over heterogeneous catalysts. *Chem. Sci.* **2015**, *6*, 4403–4425.
- (28) Xu, J.; Saeys, M. Improving the coking resistance of Ni-based catalysts by promotion with subsurface boron. *J. Catal.* **2006**, 242, 217–226.
- (29) Peng, Z.; Somodi, F.; Helveg, S.; Kisielowski, C.; Specht, P.; Bell, A. T. High-resolution in situ and ex situ TEM studies on graphene formation and growth on Pt nanoparticles. *J. Catal.* **2012**, 286, 22–29.
- (30) Helveg, S.; López-Cartes, C.; Sehested, J.; Hansen, P. L.; Clausen, B. S.; Rostrup-Nielsen, J. R.; Abild-Pedersen, F.; Nørskov, J. K. Atomic-scale imaging of carbon nanofibre growth. *Nature* **2004**, 427, 426–429.
- (31) De Jong, K. P.; Geus, J. W. Carbon Nanofibers: Catalytic Synthesis and Applications. *Catal. Rev.* **2000**, *42*, 481–510.
- (32) Sharma, R.; Moore, E.; Rez, P.; Treacy, M. M. J. Site-Specific Fabrication of Fe Particles for Carbon Nanotube Growth. *Nano Lett.* **2009**, *9*, 689–694.
- (33) Yoshida, H.; Takeda, S.; Uchiyama, T.; Kohno, H.; Homma, Y. Atomic-Scale In-situ Observation of Carbon Nanotube Growth from Solid State Iron Carbide Nanoparticles. *Nano Lett.* **2008**, *8*, 2082–2086.

- (34) Kresse, G.; Furthmüller, J. Efficient iterative schemes for ab initio total-energy calculations using a plane-wave basis set. Phys. Rev. B 1996, 54, 11169-11186.
- (35) Kresse, G.; Hafner, J. Ab initiomolecular dynamics for liquid metals. Phys. Rev. B 1993, 47, 558-561.
- (36) Kresse, G.; Hafner, J. Norm-conserving and ultrasoft pseudopotentials for first-row and transition elements. J. Phys.: Condens. Matter 1994, 6, 8245-8257.
- (37) Perdew, J. P.; Burke, K.; Ernzerhof, M. Generalized Gradient Approximation Made Simple. Phys. Rev. Lett. 1996, 77, 3865-3868.
- (38) Taylor, A. Lattice parameters of binary nickel cobalt alloys. J. Inst. Met. 1950, 77, 585-594.
- (39) Kibsgaard, J.; Tsai, C.; Chan, K.; Benck, J. D.; Nørskov, J. K.; Abild-Pedersen, F.; Jaramillo, T. F. Designing an improved transition metal phosphide catalyst for hydrogen evolution using experimental and theoretical trends. Energy Environ. Sci. 2015, 8, 3022-3029.
- (40) Monkhorst, H. J.; Pack, J. D. Special points for Brillouin-zone integrations. Phys. Rev. B 1976, 13, 5188-5192.
- (41) Henkelman, G.; Uberuaga, B. P.; Jónsson, H. A climbing image nudged elastic band method for finding saddle points and minimum energy paths. J. Chem. Phys. 2000, 113, 9901-9904.
- (42) Chase, M. W. JANAF Thermochemical Tables, 4th Edition. J. Phys. Chem. Ref. Data Monographs 1998, No. 9.
- (43) John, M.; Alexopoulos, K.; Reyniers, M.-F.; Marin, G. B. Reaction path analysis for 1-butanol dehydration in H-ZSM-5 zeolite: Ab initio and microkinetic modeling. J. Catal. 2015, 330, 28-45.
- (44) Ma, H.; Schneider, W. F. Plasma-catalyst modeling for materials selection: challenges and opportunities in nitrogen oxidation. J. Phys. D: Appl. Phys. 2021, 54, 454004.
- (45) Ma, H.; Schneider, W. F. DFT and microkinetic comparison of Pt, Pd and Rh-catalyzed ammonia oxidation. J. Catal. 2020, 383, 322-
- (46) Ma, H.; Sharma, R. K.; Welzel, S.; van de Sanden, M. C. M.; Tsampas, M. N.; Schneider, W. F. Observation and rationalization of nitrogen oxidation enabled only by coupled plasma and catalyst. Nat. Commun. 2022, 13, 402.
- (47) Ko, J.; Ma, H.; Schneider, W. Supporting Information for Kinetic origins of high selectivity of metal phosphides for ethane dehydrogenation. 2022; DOI: 10.5281/zenodo.6609601.
- (48) Nørskov, J. K.; Studt, F.; Abild-Pedersen, F.; Bligaard, T. Fundamental Concepts in Heterogeneous Catalysis; John Wiley & Sons: Hoboken, NJ, 2014.
- (49) Grabow, L. C. Computational Catalyst Screening In Computational Catalysis; The Royal Society of Chemistry: London, 2014; Chapter 1,
- (50) Abild-Pedersen, F.; Nørskov, J. K.; Rostrup-Nielsen, J. R.; Sehested, J.; Helveg, S. Mechanisms for catalytic carbon nanofiber growth studied by ab initio density functional theory calculations. Phys. Rev. B 2006, 73, 115419.
- (51) Zhao, Z.-J.; Chiu, C.-c.; Gong, J. Molecular understandings on the activation of light hydrocarbons over heterogeneous catalysts. Chem. Sci. 2015, 6, 4403-4425.

□ Recommended by ACS

Relationship between the Surface Reconstruction of Nickel Phosphides and Their Activity toward the Hydrogen **Evolution Reaction**

Sayan Banerjee, Andrew M. Rappe, et al.

MARCH 21, 2023

ACS CATALYSIS

RFAD 🗹

Insights into the Origin of High Activity of Ni₅P₄(0001) for **Hydrogen Evolution Reaction**

Yang Yang, Wen-Feng Lin, et al.

MARCH 09, 2023

THE JOURNAL OF PHYSICAL CHEMISTRY C

READ M

The Promoting Role of Ni on In₂O₃ for CO₂ Hydrogenation to **Methanol**

Francesco Cannizzaro, Ivo A. W. Filot, et al.

JANUARY 18, 2023

ACS CATALYSIS

RFAD 17

Insights into the Nature of Selective Nickel Sites on Ni/Al₂O₃ **Catalysts for Propane Dehydrogenation**

Rui Ma, Guojun Zou, et al.

OCTOBER 03, 2022

ACS CATALYSIS

READ **C**

Get More Suggestions >